

1 **Large-scale coupled hydrologic and hydraulic modelling of the Ob river in**  
2 **Siberia**

3  
4

5 Sylvain Biancamaria <sup>a,\*</sup>, Paul D. Bates <sup>b</sup>, Aaron Boone <sup>c</sup>, Nelly M. Mognard <sup>a</sup>

6  
7  
8

9 Affiliations:

10

11 (a) Université de Toulouse; UPS (OMP-PCA); LEGOS; 14 Av. Edouard Belin, F-31400  
12 Toulouse, France.

13

14 (b) School of Geographical Sciences, University of Bristol, University road, Bristol, BS8 1SS,  
15 United Kingdom

16

17 (c) GAME/CNRM, Météo-France, CNRS, 42 Av. G. Coriolis, 31057 Toulouse Cedex, France

18

19

20

21 \* Corresponding author. Tel.: +335 61 33 29 30; fax: +335 61 25 32 05. Email:

22 [sylvain.biancamaria@legos.obs-mip.fr](mailto:sylvain.biancamaria@legos.obs-mip.fr) (S. Biancamaria)

23 Abstract

24

25 The Ob river in Western Siberia is one of the largest rivers in the Arctic and has a  
26 complex hydrological cycle mainly driven by snow melting in spring and rainfall and  
27 evapotranspiration in summer/autumn. The Ob is a source of fresh water for the Arctic Ocean  
28 and a change in its regime could affect the ocean thermohaline circulation. Due to the scarcity  
29 of in situ measurements in the Arctic and the size of the region, the hydrological modelling of  
30 large Arctic rivers is difficult to perform. To model the northern part of the Ob river basin, the  
31 land surface scheme ISBA (Interactions between Soil-Biosphere-Atmosphere) has been  
32 coupled with the flood inundation model LISFLOOD-FP. Different sensitivity tests on input  
33 data and parameters have been performed and the results have been compared with in-situ  
34 measurements and remotely sensed observations of water level. The best modelling is  
35 obtained with a river depth of 10 meters and a Manning coefficient of 0.015: correlation and  
36 Nash-Sutcliffe coefficients with in-situ measurement are equal or even slightly above  
37 (depending on the precipitation dataset used) 0.99 and 0.95 respectively. The sensitivity tests  
38 show that modelling errors are mainly linked with atmospheric input (snow and rain  
39 precipitation), snow cover and drainage parameterization for ISBA and Manning coefficient,  
40 river depth and floodplain topography for LISFLOOD-FP.

41

42

43

44 Keywords: arctic, Ob river, hydraulic-hydrologic modelling, ISBA, LISFLOOD-FP, GSWP2

## 45 1. Introduction

46

47 Global warming is expected to be most significant in the boreal regions and could  
48 greatly affect the discharge regime of arctic rivers (Meehl et al., 2007). The IPCC report,  
49 Meehl et al. (2007), stated that, for this century, temperature and precipitation in arctic  
50 regions will increase significantly. Already, an increase in arctic river flow has been observed  
51 by Peterson et al. (2002) and a modification in the arctic hydrological cycle could have a  
52 feedback on the whole climate through increased input of fresh water to the Arctic Ocean.  
53 However, since the early 1990's, the number of operational gauging stations has decreased  
54 markedly in the arctic, and especially for river basins located in the former USSR  
55 (Shiklomanov et al., 2002). For this reason the use of models and satellite measurement in  
56 conjunction with the few gauging station data sets still available is crucial to the ongoing  
57 study of arctic rivers to determine how they may respond to global warming. The purpose of  
58 this paper is to model the large scale hydrology and hydraulics of an arctic river using  
59 currently available data to identify where satellite measurements and models require  
60 improvement to address the above research questions. For this study the Ob river has been  
61 chosen as it is one of the biggest arctic rivers (the third largest in terms of discharge, Herschy  
62 and Fairbridge, 1998) and because it contributes nearly 15% of total freshwater flow into the  
63 Arctic Ocean (Grabs et al., 2000).

64 Previous attempts to model the hydrological cycle of arctic rivers have mostly used  
65 climate models applied at a regional and/or global scales. Such schemes can model the annual  
66 and seasonal flows at a basin scale (Decharme and Douville, 2007) and the global water  
67 fluxes at a regional scale (Su et al., 2006), or assess the influence of permafrost (Arzhanov et  
68 al., 2008) and artificial reservoirs on the global run-off (Adam et al., 2007). The main interest  
69 in using regional and global climate models is therefore their ability to estimate the effect of

70 global warming on the hydrology of the Arctic rivers (Nohara et al., 2006; Manabe et al.,  
71 2004) using the IPCC scenarios, however they cannot so easily be used to simulate how basin  
72 hydrology interacts with surface water flow through the river network and across complex  
73 floodplains. By contrast, there are very few attempts at modelling Arctic rivers using  
74 hydrodynamic models and these have been done for rivers smaller than the Ob, where it is  
75 easier to acquire in-situ data, such as the Peace-Athabasca Delta (Peters et al., 2006). For the  
76 Amazon, it has been shown that a hydrodynamic model can successfully model the river  
77 discharge and floodplain dynamics (Wilson et al., 2007) at regional scales. However, to the  
78 author's knowledge, the present study is one of the very first to model a large scale Arctic  
79 river with a coupled hydraulic-hydrologic model.

80 The paper is organised as follows. The study domain, the models and the input data  
81 used to simulate the hydrology of the Lower Ob river are presented in section 2. The results of  
82 the modelling and the sensitivity tests are described in section 3. Further improvements and  
83 perspectives on this work are discussed in the conclusions.

84

## 85 2. Methodology

86

### 87 2.1. Study domain and time period

88

89 The study domain corresponds to the Lower Ob River between the cities of Belogorje  
90 and Salekhard, which represents roughly the last 900 km of the river before the Ob estuary  
91 (Fig. 1) and corresponds to a drainage area of 790 000 km<sup>2</sup> (from the Arctic Rapid Integrated  
92 Monitoring System, ArcticRIMS, <http://rims.unh.edu>). The Ob river is located in Western  
93 Siberia, east of the Ural Mountains and its drainage basin covers 2 990 000 km<sup>2</sup>. For  
94 discharge the Ob is the world's 12th biggest river and the 3rd biggest in the arctic (Herschy

95 and Fairbridge, 1998). Its discharge regime is mainly driven by snow melt and precipitation  
96 falling as rain between April and September and by rain precipitation from September to  
97 November. The strong relationship between spring discharge in May and snowmelt date and  
98 winter snow depth has been analysed using remote sensing techniques (Grippa et al., 2005;  
99 Yang et al., 2007). The study domain is classified as sporadic and discontinuous permafrost  
100 (Brown et al., 1998).

101 According to Serreze et al. (2002), precipitation in the Ob basin is at a maximum in  
102 summer. but is smaller than the evapotranspiration rate. Indeed, due to high  
103 evapotranspiration rates, about 25% of the July precipitation is associated with the recycling  
104 of water vapor evaporated within the domain, which shows the significant effect of the land  
105 surface (and therefore vegetation) on the summer hydrologic regime.

106 The Ob is frozen from November to April, and thawing occurs gradually during May  
107 (Pavelsky and Smith, 2004). During the thawing period some parts of the river can still be  
108 frozen, whilst the ice thawing in the most southern part creates ice jams further north which  
109 leads to widespread inundation, mainly at the tributary confluences (Pavelsky and Smith,  
110 2004). Because the Ob is a “northward-flowing” river, the upper Ob ice cover breaks up  
111 around late April to May, whereas the break up occurs around late May to early June for the  
112 lower Ob (Yang et al., 2004). Especially, at Salekhard, near the Ob mouth, the river is  
113 covered with ice during 200 days per year in average and the spring ice break up happens  
114 approximately between May 20<sup>th</sup> and June 10<sup>th</sup> (Vuglinsky, 2001). Because of this delay in  
115 ice break up between the South and North parts of the basin, the lower Ob basin receives  
116 upstream runoff contribution and stores the flow in the main river valley above its mouth,  
117 resulting in widespread flooding in May over the northern parts of the Ob. According to  
118 Beltaos and Prowse (2008), ice flow produces significant hydrologic effects that often exceed  
119 in magnitude and frequency those occurring under open-water conditions. The impact of ice

120 jam is even more important as it occurs during the annual peak flow, leading to important  
121 erosive event (Prowse, 2001). Moreover, Smith and Alsdorf (1998) highlight that spring  
122 floods are a major source of sediment deposit in the Ob floodplain.

123         Analysis of monthly streamflow records for the major subbasins within the Ob river  
124 watershed during the 1936-1990 time period has been performed by Yang et al. (2004) to  
125 examine discharge changes induced by human activities and natural variations. Yang et al.  
126 (2004) found that over the upper Ob basin there is a decreasing streamflow trend for the  
127 summer months and an increasing streamflow trend during the winter season. The decreasing  
128 trend in summer is mainly due to water use along the river valley for agricultural and  
129 industrial purposes and because of reservoir regulation to reduce the summer peak floods. The  
130 increasing trend in winter streamflow is caused by reservoir management and the release of  
131 water for power generation. By contrast, in the lower Ob basin, streamflow increased during  
132 midsummer and winter months and weakly decreased in autumn. These increases in summer  
133 flow were associated with increases in summer precipitation and winter snow cover over the  
134 northern Ob basin. So according to Yang et al. (2004), human activity can significantly  
135 impact the Ob discharge for the upper basin, however this is not an issue for the study  
136 presented here as only the lower Ob has been considered. Here the impact of reservoir and  
137 human activity is already taken into account in the observed discharge data from the  
138 Belogorje gauging station (Fig. 1) which is used as boundary condition (i.e. as a proxy of the  
139 incoming discharge to our study domain from the upstream river).

140         The aim of the work presented here is to simulate a complex river system where the  
141 flow greatly depends on the correct simulation of snow accumulation during the winter and  
142 the onset of snow melt.

143         The study time period is 1993 as it corresponds to the year when the ISBA  
144 atmospheric inputs (1982-1994), the daily discharge measured at Belogorje (January 1993 -

145 October 1994) and the satellite altimetry data (since August 1992 up to now) are  
146 simultaneously available.

147

## 148 2.2. River model (LISFLOOD-FP)

149

150 The river is modelled by the flood inundation model LISFLOOD-FP developed at the  
151 University of Bristol (Bates and De Roo, 2000). It predicts water depth in each grid cell at  
152 each time step and hence can simulate the dynamic propagation of flood waves over fluvial,  
153 coastal and estuarine floodplains. LISFLOOD-FP is a coupled 1D/2D hydraulic model based  
154 on a raster grid. The 1D channel flow is based on the kinematic approximation to the 1D St  
155 Venant equations. Floodplain flows are similarly described in terms of continuity and  
156 momentum equations, discretized over a grid of square cells, which allows the model to  
157 represent 2-D dynamic flow fields on the floodplain. However there is no exchange of  
158 momentum between main channel and floodplain flows, only mass.

159 Fig. 2 shows all the data required to run LISFLOOD-FP. The main input data are the  
160 floodplain topography from a Digital Elevation Model (DEM) and the river centreline co-  
161 ordinates along with its width and depth. For this study the Manning coefficients for the river  
162 and for the floodplain have also been assumed constant in space and time. The incoming flow  
163 to the study domain from the upstream river is given by the daily discharge measured at the  
164 Belogorje gauging station (Fig. 1). The lateral inflows to the river in the study domain are  
165 computed by ISBA (Interactions between the Soil-Biosphere-Atmosphere, Noilhan and  
166 Mahfouf, 1996), which is a Land Surface Scheme (LSS) developed by the CNRM (Centre  
167 National de Recherche Meteorologique), see paragraph 2.3 for more detail. In this study, there  
168 are eight lateral inflows (Fig. 1). Finally, LISFLOOD-FP provides water height and discharge  
169 outputs for each point of the channel and for each grid cell on the floodplain.

170

## 171           2.3. Lateral inflows

172

173           Lateral inflows are a critical input for large area hydraulic models, and especially for  
174 arctic rivers where snow melt is the main driver of the river regime. They represent water  
175 from run-off and the drainage from the whole watershed to the river. Yet, no in-situ or remote  
176 sensing data are available to measure these contributions, so they can be estimated only by the  
177 combination of a LSS, which computes the surface water available at each grid cell of the  
178 basin and a routing scheme, which routes the surface water leaving each grid cell to the river.  
179 The next paragraphs present the LSS and the routing scheme used in this study.

180

## 181                   2.3.1. ISBA

182

183           ISBA (Noilhan and Mahfouf, 1996) is a LSS with an explicit snow modelling  
184 component (Boone and Etchevers, 2001) and can simulate deep soil freeze-thaw cycles  
185 (Boone et al., 2000). Accurate snow pack modelling is of great importance to simulation of an  
186 arctic river and explain why ISBA has been chosen for this work. Moreover, ISBA has been  
187 used with the explicit soil diffusion option (Boone et al., 2000), which means the soil is  
188 explicitly modelled and is discretized into five layers with the highest vertical resolution at the  
189 surface. This option allows a more realistic simulation of the near-surface soil temperature  
190 gradient and freeze–thaw cycles than the classical force-restore option, see Boone et al.  
191 (2000) for more details. Moreover, the ISBA version used in this study includes a sub-grid  
192 runoff scheme (Habets et al., 1999).

193           Another key issue to estimate correctly the lateral inflows from ISBA to LISFLOOD-  
194 FP is the atmospheric data used as an ISBA input. In this study, forcing data comes from the

195 Global Soil Wetness Project – Phase II (GSWP2; Dirmeyer et al., 2006). GSWP2 aims to  
196 foster the development of LSSs and to assess the quality of their performance as well as that  
197 of the forcing datasets used to drive them. Therefore, different precipitation (rain and snow)  
198 datasets has been developed by GSWP2. These are based on two different reanalysis  
199 precipitation datasets: NCEP/DOE (Kanamitsu et al., 2002) and ERA-40 (Betts and Beljaars,  
200 2003). Then, two corrections can be applied to these precipitation fields: hybridization  
201 (correction using gauge and satellite based precipitation data) and correction for gauge under-  
202 catch (Dirmeyer et al., 2006). For the first correction (hybridization), two observational  
203 precipitation datasets can be used: the gauge-based Global Precipitation Climatology Centre  
204 (GPCC, Rudolf et al., 1994) and the satellite-based Global Precipitation Climatology Project  
205 (GPCP, Huffman et al. 1997), leading to different hybridization corrections (Dirmeyer et al.,  
206 2006). GSWP2 has defined several experiments by combining the two precipitation datasets  
207 with the different corrections (Table 1). Decharme and Douville (2006) compared multi-  
208 model outputs forced with GSWP2-B0 and GSWP2-P3 on the French part of the Rhône river  
209 basin. Compared to an observation-based dataset, they concluded that GSWP2-P3 gives better  
210 results than GSWP2-B0. For this reason in this study the GSWP2-P3 forcing field has been  
211 used for the nominal run.

212 ISBA was run with the same  $1^{\circ} \times 1^{\circ}$  spatial resolution as the GSWP2 forcing data and  
213 used to compute the run-off (surface water) and drainage (sub-surface water) leaving each  
214  $1^{\circ} \times 1^{\circ}$  grid cell. Yet, as each ISBA grid cell is spatially independent and not coupled laterally  
215 with any other, a routing scheme is required to bring to the river the water which leaves each  
216 pixel.

217

218 2.3.2. Routing Scheme

219

220 The routing scheme used to route the run-off and drainage from each ISBA pixel to  
221 the river is the Total Runoff Integrating Pathways (TRIP; Oki and Sud, 1998) algorithm.  
222 TRIP is a global river channel network at  $1^{\circ} \times 1^{\circ}$  resolution, extracted from the ETOPO5 DEM  
223 and publicly available from <http://hydro.iis.u-tokyo.ac.jp/~taikan/TRIPDATA/>. TRIP gives  
224 the flow direction from each pixel with the three following constraints:

- 225 1. No river channels are allowed to cross.
- 226 2. All river channels flow from one land grid box to another.
- 227 3. Every land grid box has one, and only one, river mouth toward its downstream.

228 Fig. 3 shows the routing scheme derived from TRIP to route the water computed from  
229 each ISBA pixel within the drainage area to an ISBA pixel which contains a segment of the  
230 lower Ob (blue dots on the Fig. 3). These amounts of water represent the lateral inflows to the  
231 river computed from ISBA+TRIP. Finally, each lateral inflow is inserted as a point source  
232 into LISFLOOD-FP at the point along the river vector which is closest to the center of the  
233 blue ISBA grid cells in Fig. 3 (i.e. the whole model unit is assigned to one point along the  
234 LISFLOOD-FP reach).

235

## 236 2.4. Ancillary data

237

### 238 2.4.1. Gauge data

239

240 In this study discharge from two gauging stations are used (see Fig. 1 for their  
241 location). The first one, at Belogorje, is used to estimate the incoming upstream flow to the  
242 study domain. The second one at Salekhard is used to validate the modelled discharge.  
243 Discharge time series for these two gauging stations have been downloaded from the  
244 ArcticRIMS website (<http://rims.unh.edu>).

245

246

#### 2.4.2. Channel topography and parameters

247

248

249

250

251

252

253

254

255

256

257

258

259

The river centreline has been extracted from the CIA World Data Bank II river mask (Gorny and Carter, 1987). From this river vector, it has been estimated that the average distance along the river between two lateral inflows is around 140 km. However the river depth and width are not well known along the river. From Landsat images, the mean river width for the Lower Ob is around 2 km, yet with large variability at some locations. Thus, the river width along the Ob has been considered constant and equal to 2 km (two pixels of the floodplain topography, see section 2.4.3). A previous study from Akimenko et al. (2001) stated that maximum depths on the lower Ob can reach 15m to 20m. To estimate the channel topography, it has been assumed that river bed elevation corresponds to the smoothed DEM elevation along the river centre minus a constant river depth (Fig. 4). To test the uncertainty in the river depth, four different values (5m, 10m, 15m and 20m) of river depth have been used and simulations run with each of these.

260

261

262

263

264

265

The Manning coefficient (or friction coefficient) for the river is not well known, however for a river channel with a sand bed and no vegetation the Manning coefficient is known to vary from 0.011 to 0.035 (Chow, 1964). So, to simplify the modelling, the channel Manning coefficient has been set to a constant value in space and time and several runs have been done with different plausible value (from 0.01 to 0.04 in steps of 0.005).

266

#### 2.4.3. Floodplain topography and parameters

267

268

269

For high latitudes very few DEMs are available. The best ones are ACE (Altimeter Corrected Elevation) from De Montfort University and GTOPO30 from the USGS (United

270 States Geological Survey). Both have a 30 arc-seconds (~1km) spatial resolution, which is  
271 therefore the LISFLOOD-FP output spatial resolution. Yet, after plotting the two DEM (Fig.  
272 5), it becomes obvious that they have artefacts which will greatly affect the simulated  
273 floodplain inundation. Indeed, on the study domain below 66°N, ACE has been generated by  
274 interpolating ERS-1 data from its geodetic mission. Above 66°N, it uses the same data as  
275 GTOPO30. Fig. 5a shows the interpolation artefacts (where the satellite ground tracks can be  
276 seen). For GTOPO30, the data come from different Digital Terrain Elevation Data (DTED),  
277 with different resolutions and qualities. This is why sometimes there is an obvious offset due  
278 to change of data sources, as is clearly shown in Fig. 5a around 64°N. Because of these offsets  
279 and because GTOPO30 has a constant value in the river floodplain between 62.3°N and  
280 almost 64°N (Fig. 5a), using this DEM gives non realistic floodplain water depths in the  
281 LISFLOOD-FP model (Biancamaria et al., 2007). For these reasons the ACE DEM has been  
282 chosen for our modelling as it represents the best of the poor terrain datasets available. The  
283 Manning coefficient for the floodplain has been assumed constant in space and time and equal  
284 to 0.06.

#### 286 2.4.4. ISBA vegetation parameters

287  
288 In this study the vegetation and soil parameters (Leaf Area Index (LAI), Vegetation  
289 cover fraction, non-snow-covered surface all-wavelength albedo and non-snow-covered bare  
290 soil-vegetation roughness length) used as input to ISBA come from Ecoclimap (Masson et al.,  
291 2002). Ecoclimap is a monthly global surface parameter dataset at 1-km resolution and has  
292 been derived by combining existing land cover and climate maps, in addition to using  
293 Advanced Very High Resolution Radiometer (AVHRR) satellite data. This dataset has been  
294 resampled at 1°x1° spatial resolution for the study domain.

295 Another vegetation cover and LAI dataset, from the University of Wales, is also  
296 available and has been used by GSWP2. It has been computed from Pathfinder Advanced  
297 Very High Resolution Radiometer (AVHRR) Land (PAL) channel 1 and 2 data, and corrected  
298 for Bidirectional Reflectance Distribution Function (BRDF) effects, volcanic aerosols, cloud  
299 and atmospheric effects and missing data. This dataset has a monthly time resolution and is  
300 available for the years 1982 to 1998. This second set of vegetation data has been used in this  
301 study to investigate the sensitivity of the modelling to the vegetation parameters.

302

### 303 3. Results and sensitivity tests

304

305 The hydrology of the Ob basin, as modelled by ISBA, is first described and issues  
306 with modelled lateral inflows are discussed and investigated. Sensitivity to ISBA vegetation  
307 and drainage parameters, and to precipitation input is studied in section 3.1. Sensitivity to  
308 LISFLOOD-FP parameters, like river depth and Manning coefficient, is addressed in section  
309 3.2. Lastly, model validation for a nearly ungauged river like the Ob is a very tricky task. For  
310 this reason the chosen model validation strategy is as follow: modelled outputs from  
311 ISBA/LISFLOOD-FP are first compared to in-situ measurement and then water elevations  
312 modelled by LISFLOOD-FP are compared to Topex/POSEIDON data.

313

#### 314 3.1. Sensitivity to ISBA inputs and parameters

315

##### 316 3.1.1. Modelled Ob basin hydrology

317

318 Based on energy budgets and parameterization of physical processes, ISBA modelled  
319 the physical hydrology of the lower Ob. In particular, the use of a three layers snow scheme

320 and an explicit five layers soil, with a freezing module (allowing modelling of permafrost  
321 conditions), is well suited to simulation of high latitude hydrology. Since ISBA is used to  
322 compute the lateral inflows to the river, its value can be validated by a simple computation of  
323 the difference between the measured discharge at the Belogorje and Salekhard gages. Yet, as  
324 there are 900km between Belogorje and Salekhard, there is a time lag between the two  
325 measured discharges. The computation of the cross-correlation between measured time-series  
326 at Belogorje and at Salekhard shows that the peak discharge at Belogorje occurs 10 days  
327 before the peak discharge at Salekhard (Fig. 6a). The difference between Salekhard discharge  
328 and a 10 days-time-lag Belogorje discharge shows that the total lateral inflows between the  
329 two gages has a maximum value of 12 000 m<sup>3</sup>/s occurring between the end of May and the  
330 beginning of June (Fig. 6a and 6b). However, the sum of all the lateral inflows modelled by  
331 ISBA has a maximum of 8 000 m<sup>3</sup>/s and occurs between the end of March and the beginning  
332 of April (fig 6b). Therefore, the peak in modelled lateral inflows is not only underestimated  
333 but occurs almost two months in advance compared to in-situ measurements. Fig. 6c shows  
334 the modelled discharge time-series for each lateral inflow. There are three predominant lateral  
335 inflows: lateral inflow numbers 2, 6 and 8 (see Fig. 3 for their location). Whilst these all have  
336 a discharge maximum at the end of March, lateral inflow n°6 is the major contributor to the  
337 peak in the sum of all the modelled lateral inflows which occurs during the March/April  
338 period.

339 To investigate the cause of this early modelled lateral inflows, different hydrological  
340 variables modelled by ISBA have been plotted on Fig. 7. All the plots on this figure  
341 correspond to spatial averages over all the ISBA grid cells contributing to lateral inflow n°6  
342 (see Fig. 3 for the location of these grid cells). For the year 1993, rain precipitation mostly  
343 occurs between June and October (Fig. 7a), with a mean value of 0.9 mm/day and a maximum  
344 value of 11 mm/day. Snow precipitation occurs from January to May and September to

345 December 1993 (Fig. 7b), with a mean value of 0.9 mm/day and a maximum value of 6.5  
346 mm/day. The evapotranspiration (Fig. 7c) is important in summer (between June and  
347 September) with a mean value of 1.6 mm/day and a maximum value of 3.9 mm/day (during  
348 this period the mean rain precipitation rate is just a bit smaller than 1.6 mm/day). During the  
349 rest of the year, evapotranspiration is very small. These results are quite similar, yet slightly  
350 lower, than the ones from Serreze et al. (2002) for the entire Ob basin (precipitation rate of  
351 1.9 mm/day and evapotranspiration of 2 mm/day in summer). Surprisingly, snow fraction  
352 (Fig. 7d), which is the fraction of snow covering a grid cell, is very small and never exceeds  
353 0.17. This means that less than 17% of the area of each grid cell contributing to lateral inflow  
354 is covered by snow during winter time. This is due to the ISBA sub-grid snow fraction  
355 parameterization, which considers that the snow cover fraction generally stays relatively low  
356 when tall vegetation is present, in order to represent vegetation elements protruding through  
357 the snowpack. This small snow fraction has two effects: first, soil is not isolated from the air  
358 temperature during winter and second, the albedo of the surface is lower and so it can be  
359 warmed more rapidly by incoming solar radiation. Therefore, modelled temperature in the  
360 first soil layer (Fig. 7f) is almost exactly the same as the as air temperature (Fig. 7e). Thus,  
361 when air temperature rises in March and becomes above 0°C for 5 consecutive days, ground  
362 temperature rapidly acquires the same value, leading to the melt of nearly all the snowpack in  
363 March. Finally, Fig. 7g and 7h present the total liquid water equivalent soil ice and soil liquid  
364 water content, respectively. Contrary to snow, soil ice barely decreases during mid-March  
365 when soil temperature becomes above 0°C for a few days. Soil ice content really begins to  
366 decrease in mid-April, when soil temperature is equal or above 0°C for a longer period and  
367 when there is almost no more snow to absorb heat. Soil ice completely disappears between  
368 July and September. Soil water content, which is small in winter, increases rapidly during  
369 mid-March snow melt and after mid-April, with two local maxima in July and October.

370

371

### 3.1.2. Sensitivity to the snow fraction parameters

372

373

374

375

376

377

The discharge peak in March in the modelled lateral inflows is mainly due to an early snow melt caused by a small snow fraction modelled by ISBA. The total snow fraction ( $p_n$ ) computed by ISBA is a weighted sum (Eq. 3) of the snow fraction over vegetation ( $p_{nc}$ , Eq. 1) and over bare soil ( $p_{ng}$ , Eq. 2), see Pitman et al. (1991) for more information about Eq. (1) and Eq. (2).

378

$$p_{nc} = \left( \frac{D_s}{D_s + c_{pn} Z_0} \right)^{b_{pn}} \quad (0 \leq p_{nc} \leq 1) \quad (1)$$

379

$$p_{ng} = \left( \frac{W_s}{a_{pn} W_s + W_{np}} \right)^{b_{pn}} \quad (0 \leq p_{ng} \leq 1) \quad (2)$$

380

$$p_n = (1 - veg) \cdot p_{ng} + veg \cdot p_{nc} \quad (3)$$

381

382

383

384

385

386

where  $D_s$  is the snow depth computed by ISBA,  $W_s$  is the snow water equivalent (SWE) computed by ISBA,  $W_{np}$  is the generalized critical SWE ( $W_{np}=10 \text{ kg.m}^2$ ),  $a_{pn}=1$ ,  $b_{pn}=1$ ,  $c_{pn}=5$ ,  $Z_0$  is the soil/vegetation roughness length and  $veg$  is the vegetation fraction cover. This is a fairly standard sub-grid parameterization which was developed for use in large scale General Circulation Model (GCM) applications (see Wu and Wu, 2004, for a review of such schemes).

387

388

389

390

391

$Z_0$  and the vegetation cover are climatological monthly varying ISBA inputs. The mean value of the vegetation cover (from ECOCLIMAP) for all the grid cells contributing to lateral inflow 6 is equal to 0.94 (Fig. 8a). In ECOCLIMAP, those grid cells are classified as forest, and consequently  $Z_0$  is relatively high (between 1.32 and 1.36 m). This means that, given the value of  $Z_0$ , snow fraction over vegetation is quite small (around 0.15, Fig. 8b) and,

392 because vegetation cover is close to 1, the total snow fraction is almost equal to the snow  
393 fraction over vegetation (Eq. 3), which explains the small value of the total snow fraction.  
394 There are two solutions to this issue: 1- vegetation fraction cover is not realistic and should be  
395 decreased and/or 2- the snow fraction of vegetation is not realistic and should be increased.  
396 Solution 1 does not seem to be the most likely, as the vegetation cover is based on actual  
397 satellite data. To test the sensitivity of the modelling to the vegetation cover, vegetation  
398 parameters from ECOCLIMAP have been replaced by the dataset from the University of  
399 Wales (see section 2.4.4). Yet, modelled lateral inflows were still very similar, with an early  
400 snowmelt in March. By contrast, solution 2 might be the most likely, because there is more  
401 uncertainty in the parameterization of  $p_{nc}$ . Indeed, from Eq. (1) it is clear that snow fraction  
402 over vegetation is a function of SWE and  $Z_0$ , whereas snow fraction over bare soil (Eq. 2) is  
403 only a function of SWE (or snow depth). The basic idea behind this parameterization is that  
404 bare ground is more quickly covered with snow than areas with high vegetation (like forests).  
405 Thus, if  $Z_0$  is high, as it is the case here, snow fraction over vegetation will be low. Yet, this  
406 behavior depends on the coefficients in Eq. (1) and especially  $c_{pn}$ . Even if Eq. (1) and Eq. (2)  
407 are commonly used by LSSs like ISBA, the value of their coefficients is very empirical with  
408 huge uncertainties and therefore is highly variable between different models (Pitman et al.,  
409 1991; Verseghy, 1991; Yang et al., 1997). Thus, the  $c_{pn}$  coefficient can be tuned to obtain a  
410 better timing in the modelled snow melting.

411         The high value of  $Z_0$  might not be completely realistic when there is snow. Indeed,  
412 pure snow has a very small roughness length, around 0.001 m. So, the “true” roughness length  
413 of a grid cell should be reduced when there is snow. A simple way to take this physical  
414 process into account is to do a nonlinear average of a snow roughness for a pure snow surface  
415 and the initial value of  $Z_0$  (Eq. 4 and Eq. 5). This kind of average is commonly used for  
416 roughness length computation (Noilhan and Lacarrère, 1995).

$$Z_{0n} = p_n \frac{1}{\left[ \ln \left( \frac{0.001}{P_{zref}} \right) \right]^2} + (1 - p_n) \frac{1}{\left[ \ln \left( \frac{Z_0}{P_{zref}} \right) \right]^2} \quad (4)$$

418

$$Z_{0new} = P_{zref} \cdot \exp \left( \frac{-1}{\sqrt{Z_{0n}}} \right) \quad (5)$$

420

421

422

423

424

425

426

427

428

429

430

431

432

433

434

435

436

437

438

Fig. 9 shows the lateral inflows computed from ISBA for  $c_{pn}$  equal to 5 (nominal value), 1, 0.1, 0.01 and 0.001, for a roughness length equal to  $Z_0$  (Fig. 9a) and to  $Z_{0new}$  (Fig. 9b). The higher the values of the  $c_{pn}$  coefficient yield, the better the timing of the modelled lateral inflow sum. Yet, the maximum modelled total inflow can be very high and the base flow is still very low. For  $Z_{0new}$ , increasing  $c_{pn}$  above 0.01 does not significantly change the total lateral inflow. Besides, total lateral inflow with  $Z_{0new}$  and  $c_{pn}$  equal to 0.01 is very close to lateral inflow with  $Z_0$  and  $c_{pn}$  equal to 0.001. Now that total lateral inflow has a good timing, it is necessary to increase the base flow and reduce the maximum discharge.

### 3.1.3. Sensitivity to drainage parameter

From Fig. 9, it is obvious that modelled lateral inflows' base flow is too small. In ISBA a parameterization has been implemented which allows the model to generate drainage or base flow even over dry soil (Etchevers et al., 2001). It assumes that when the soil water content is below a given threshold (called  $w_{drain}$ , in  $m^3/m^3$ ), the drainage is constant at a rate based on the soil texture. However, this means that there will be less water flow during wet periods. When  $w_{drain}$  is equal to 0 (like in the nominal version of ISBA used up to now) this parameterization is disabled. Fig. 10 shows the sum of all lateral inflows for  $c_{pn}=0.01$ , roughness length equal to  $Z_{0new}$  and  $w_{drain}$  equal to 0, 0.01, 0.02, 0.03 and 0.05. Clearly, for

439  $w_{\text{drain}} > 0.02$ , base flow is too high and the maximum discharge is too small. For  $w_{\text{drain}}$  equal  
440 to 0.01 and 0.02, globally base flow seems in good agreement with in-situ measurement,  
441 except during November and December when it is overestimated. For  $w_{\text{drain}}$  equal to 0.01,  
442 maximum discharge is still overestimated and delayed by a few days. On the contrary, for  
443  $w_{\text{drain}}$  equal to 0.02, maximum discharge is slightly underestimated, but still delayed  
444 compared to the difference between in-situ discharge at Salekhard and Belogorje. However,  
445 no matter the value of  $w_{\text{drain}}$ , the total lateral inflow is always underestimated between July  
446 and August. This might be due to too weak rain precipitation used as ISBA input and/or because  
447 ISBA does not model aquifer or local perched water tables, which contribute to river flow  
448 during the dry season.

#### 450 3.1.4. Sensitivity to precipitation input

451  
452 Fig. 11 shows the sum of all lateral inflows modelled by ISBA forced by the six  
453 precipitation datasets available from GSWP2 (see section 2.3.1 and Table 1) with  $c_{\text{pn}}=5$ ,  
454  $w_{\text{drain}}=0$  and  $Z_0$  (nominal run, a.) and with  $c_{\text{pn}}=0.01$ ,  $w_{\text{drain}}=0.02$  and  $Z_{0\text{new}}$  (b.). B0 and P2  
455 give similar results and greatly overestimate total lateral inflow. P4 is very similar to PE, but  
456 they are both smaller than B0 and P2, even if they still underestimate total lateral inflow. On  
457 the contrary, GSWP2-P1 and P3 are comparable and underestimate total lateral inflow.  
458 Therefore, it appears that there is a lot of variability in the modelled lateral inflows,  
459 depending on the precipitation datasets. Yet, the difference between in-situ measurements at  
460 Salekhard and Belogorje is just a rough estimate of the total lateral inflow and for a real  
461 assessment of the “best” precipitation dataset to use, it is necessary to compare the modelled  
462 discharge at Salekhard and the in-situ measurement (fig11.c and d). The modelled discharge  
463 at Salekhard is obtained for a 10 m river depth and a Manning coefficient of 0.015 (see next

464 section for a sensitivity study to these parameters). Discharge is modelled for all GSWP2  
465 precipitation datasets using two groups of parameters: 1)  $c_{pn}=5$ ,  $w_{drain}=0$  and  $Z_0$  (fig 11.c)  
466 and 2)  $c_{pn}=0.01$ ,  $w_{drain}=0.02$  and  $Z_{0new}$  (fig 11.d). As expected, for all precipitation datasets  
467 lateral inflows computed with  $c_{pn}=0.01$ ,  $w_{drain}=0.02$  and  $Z_{0new}$  are in better agreement with  
468 the difference between measured discharge at Salekhard and Belogorje than lateral inflow  
469 obtained with  $c_{pn}=5$ ,  $w_{drain}=0$  and  $Z_0$ . Table 2 presents the correlation coefficient, bias, Root  
470 Mean Square Error (RMSE) and Nash-Sutcliffe coefficient between observed and modelled  
471 discharge at Salekhard for all precipitation fields. The best results are obtained with GSWP2-  
472 P1 and P3, even if they underestimate discharge. GSWP2-P4 gives fairly good results but  
473 overestimates discharge. The worst results are obtained for GSWP2-B0 and P2 which  
474 dramatically overestimate discharge. This is coherent with the work from Decharme and  
475 Douville (2006), who also found that modelled discharge is greatly overestimated when  
476 applying correction for gauge under-catch to hybridized precipitation dataset. Moreover, they  
477 found that discharge modelled using GSWP2-P3 precipitation field is always underestimated  
478 at high latitude, which is confirmed here.

479 From these results, lateral inflows obtained with GSWP2-P3 and P4 (which are quite  
480 different but still close to in-situ measurement) and  $c_{pn}=0.01$ ,  $w_{drain}=0.02$  and  $Z_{0new}$  will be  
481 used for the sensitivity study to LISFLOOD-FP parameter in the next section.

482

### 483 3.2. Sensitivity to LISFLOOD-FP parameters

484

#### 485 3.2.1. Sensitivity to river depth and Manning coefficient

486

487 As LISFLOOD-FP assumes a rectangular channel cross section, the river depth  
488 determines the maximum discharge in the main river channel and when there will be

489 inundation. The river width plays the same role, and for this reason, to simplify the sensitivity  
490 tests, only river depth is changed. Since the Ob river depth can reach 15m and even 20m,  
491 three different values of the constant river depth (5m, 10m and 15m) have been tested. As  
492 river depth decreases, so does the capacity of the channel and more water is transferred to  
493 floodplain sections during high discharge events. This increased floodplain storage has the  
494 effect of delaying the downstream progression of the flood wave.

495         The Manning coefficient greatly impacts the flow speed, which then impacts discharge  
496 and flood extent. Indeed, the slower the flow, the more water can be accumulated and then be  
497 available for floodplain inundation. The Ob bed is mainly composed of sand (Akimenko et  
498 al., 2001) and the lower Ob is mostly a straight river, so the Manning coefficient can be  
499 chosen to be about 0.02 (Chow, 1964). Yet, at some periods of the year it can increase, for  
500 example during snow melt when the river carries ice and mud. For this reason the model has  
501 been run for four values of the channel Manning coefficient (0.01, 0.015, 0.020 and 0.025).

502         Fig. 12a and 12c present, respectively for GSWP2-P3 and GSWP2-P4 lateral inflows,  
503 the modelled discharge at Salekhard for different values of river depth (red and magenta  
504 curves) for a Manning coefficient of 0.015. On these plots, the blue curve corresponds to the  
505 measured discharge at Salekhard. These plots clearly show that for greater river depth the  
506 maximum discharge happens earlier, with a higher amplitude, than for smaller river depth.  
507 For river depths equal or above 10m, there is a good timing between modelled and in-situ  
508 discharge, for both precipitation datasets. This good agreement is mainly due to limited  
509 overbank flooding leading to attenuation of the flood wave.

510         Fig. 12b and 12d present, respectively for GSWP2-P3 and GSWP2-P4 lateral inflows,  
511 the modelled discharge at Salekhard for different values of the Manning coefficient (red and  
512 magenta curves) for a river depth of 10m. The different curves clearly show that, with a

513 higher channel Manning coefficient, the water is slowed down, which could increase  
 514 floodplain inundation and delay the modelled discharge.

515 Furthermore, for both precipitation forcing fields, there is a delay between in-situ and  
 516 modelled discharges between September and December, when discharge is only driven by  
 517 autumn rainfall. This delay is difficult to explain and could be due to a wide range of reasons:  
 518 errors in the precipitation location (for example if the location of rainfall in the GSWP2 data  
 519 set is further south, then it will take more time for the water to reach Salekhard) or in the  
 520 timing, a change in the value of the friction coefficient (in spring the friction should be higher  
 521 because of ice melting, yet the Manning coefficient is already very low), etc.

522 To find the best couples of LISFLOOD-FP parameters (Manning coefficient and river  
 523 depth), the mean error, root mean square error, correlation coefficient and Nash-Sutcliffe  
 524 coefficient have been computed (Table 3) between observed and modelled discharge for each  
 525 value of the Manning coefficient and river depth (for both GSWP2-P3, normal size numbers,  
 526 and GSWP2-P4, bold numbers). For GSWP2-P3, the best agreement between observed and  
 527 modelled discharge is obtained with a river depth of 15m and a Manning coefficient of 0.020  
 528 (the RMSE is minimized and equal to 1 956 m<sup>3</sup>/s). However, for GSWP2-P4, the best  
 529 agreement between observed and modelled discharge is obtained with a river depth of 10m  
 530 and a Manning coefficient of 0.015 (the RMSE is minimized and equal to 2 409 m<sup>3</sup>/s).

531 These values of the parameters seem reasonable for a river channel with a sand bed  
 532 and no vegetation (the Manning coefficient is known to vary from 0.011 to 0.035, Chow,  
 533 1964) and with a maximum river depth between 15m or 20m (Akimenko et al., 2001).

534

535 3.2.2. Comparison with altimetry

536

537 To estimate which averaged river depth between 10m and 15m is closer to reality, the  
538 modelled water elevations along the river channel have been compared to measured water  
539 elevations from the Topex/POSEIDON satellite radar altimeter. The location of the twenty  
540 two Topex/POSEIDON virtual stations used in this study is shown by the red dots on Fig. 13.  
541 As the lower Ob is wide (river width is around 2 km), the altimeter gives relatively good  
542 results, except in winter, when the river is frozen. For this reason the comparison between  
543 modelled and remotely sensed water heights has only been undertaken for the period May to  
544 September 1993. Whilst the ability of the LISFLOOD-FP model to match these data will be  
545 hampered by errors in the floodplain DEM, this should give some indication as to which river  
546 depth is most likely to be correct.

547 Fig. 14 shows the comparison between the height measured by Topex/POSEIDON  
548 (red curve) and the modelled height with GSWP2-P3 (magenta dashed curve) and with  
549 GSWP2-P4 (black curve) for a 10 m river depth and a 0.015 Manning coefficient at the  
550 location of Topex/POSEIDON measurements n°4 (a.), n°9 (b.), n°17 (c.) and n°24 (d.), see  
551 Fig. 13 for their location. Water heights modelled with GSWP2-P4 appear to be closer to the  
552 satellite measurement than water heights modelled with GSWP2-P3. This is due to the fact  
553 that total lateral inflow computed by ISBA using GSWP2-P4 precipitation dataset is higher  
554 than total lateral inflow obtained with GSWP2-P3. In particular, with GSWP2-P3, lateral  
555 inflow n°2 is quite small compared to lateral inflow n°6 and 8, which is not the case with  
556 GSWP2-P4, (lateral inflow n°2 has the same order of magnitude as the two other lateral  
557 inflows). Furthermore, there is no significant phase error between modelled and measured  
558 water heights.

559 Table 4 shows the mean RMSE between Topex/POSEIDON and modelled water  
560 heights for all Topex/POSEIDON stations and the four stations shown in Fig. 14, for the two  
561 best couples of river depth and Manning coefficient found in section 3.2.1 for GSWP2-P3 and

562 GSWP2-P4. Table 4 confirms the better agreement between Topex/POSEIDON and modelled  
563 water elevation for GSWP2-P4. The RMSE between altimetry measurements and modelled  
564 water heights increased with latitude especially above 65°N, which means that either the  
565 hypothesis of a constant river depth is not realistic or that the switch in the ACE DEM at  
566 66°N to use the GTOPO30 data degrades the ability of LISFLOOD-FP to predict water surface  
567 elevation. In addition, the hypothesis that each lateral inflow computed by ISBA is inserted as  
568 a single point source into LISFLOOD-FP might also explain why some RMSEs are smaller  
569 than others. In reality, a single ISBA lateral inflow might correspond to different tributaries  
570 which do not reach the main stream at the same point. Therefore, modelled water height may  
571 be different from the true one, even if channel bathymetry was perfectly known.

572 For both precipitation datasets, it appears that the best prediction of large scale flow  
573 hydraulics is obtained by using a river depth around 10m and a Manning coefficient of 0.015.

574

#### 575 4. Conclusions and perspectives

576

577 This study shows that it is possible to model discharge of a nearly ungauged arctic  
578 basin by coupling a hydrologic (ISBA) and a hydrodynamic (LISFLOOD-FP) model using  
579 simple assumptions for river parameters (constant Manning coefficient and river depth) and  
580 in-situ measurements as a proxy for the upstream flow. Different sensitivity tests on input  
581 data and parameters show that the modelling is sensitive to the atmospheric input (rain and  
582 snow precipitation), snow cover and drainage parameterization for ISBA, and to Manning  
583 coefficient and river depth for LISFLOOD-FP. The DEM is a key parameter in the discharge  
584 uncertainty as it controls floodplain water depths, hydroperiod and storage volume, which in  
585 turn influences wave propagation speeds (Biancamaria et al., 2007). The study presented here  
586 used different precipitation datasets from GSWP2 to model the lower Ob river. Best results

587 are obtained with precipitation fields which are not corrected from gauge under-catch and in  
588 particular with GSWP2-P3 and GSWP2-P4 datasets. This finding is in agreement with a  
589 previous study from Decharme and Douville (2006). Furthermore, it has been shown that a  
590 change in the value of two ISBA parameters driving soil drainage and the snow fraction over  
591 vegetation respectively, allows a better timing and amplitude of the modelled lateral inflows  
592 to the river. Comparison with in-situ measurements at the exit of the study domain and  
593 observed water heights from Topex/POSEIDON along the river has allowed to estimate the  
594 best value of the LISFLOOD-FP river depth (10 m) and Manning coefficient (0.015). With  
595 GSWP2-P3 precipitation, a 10 m river depth and a Manning coefficient of 0.015, the  
596 correlation coefficient and RMSE between modelled and observed discharge at the exit of the  
597 study domain are respectively equal to 0.99 and 1917 m<sup>3</sup>/s (which represents 14% of the mean  
598 in-situ discharge). With GSWP2-P4 precipitation and the same value of the river parameters,  
599 the correlation coefficient and RMSE between modelled and observed discharge at the exit of  
600 the study domain are respectively equal to 0.99 and 2289 m<sup>3</sup>/s (which represents 17% of the  
601 mean in-situ discharge). The RMSE between modelled and Topex/POSEIDON measured  
602 water heights along the river is equal to 2.6 m and 2.0 m for GSWP2-P3 and GSWP2-P4  
603 respectively. Yet, the value of the RMSE is relatively dependent of the location along the  
604 river.

605         The sensitivity of the modelling to the different parameters is a key factor and since  
606 there are only sparse in situ measurements, satellite estimates should be used in the future to  
607 refine some of the models parameters such as the Manning coefficient, drainage  
608 parametrization, etc to improve the models and simulate how basin hydrology interacts with  
609 surface water flow through the river network and across complex floodplains. This could be  
610 done by assimilating these satellite data both in ISBA and LISFLOOD-FP. In particular, this  
611 kind of study will greatly benefit from future wide swath altimetry, like the Surface Water and

612 Ocean Topography (SWOT) mission, planned for launch around 2013/2016. SWOT will  
613 measure 2D water heights over a 120 km wide swath and thus better constrain the models  
614 (compared to 1D measurements from nadir altimetry or in-situ measurements).

615 Finally, undertaking this type of modelling is inherently difficult as the studied  
616 processes are poorly known and interact in a complex manner. This study is one of the first to  
617 investigate the hydrodynamic modelling of the lower Ob and the results are promising. This  
618 work therefore provides a significant contribution to the understanding of modelling for a  
619 large Arctic river basin and offers new and promising perspectives.

620 Acknowledgements

621

622 The authors are greatly thankful to the ArcticRIMS project for their huge work to gather and

623 to freely distribute gauging data for the arctic regions via their website (<http://rims.unh.edu>).

624 They are also very grateful to Pr. Taikan Oki for letting TRIP data freely available for

625 download on his website (<http://hydro.iis.u-tokyo.ac.jp/~taikan/TRIPDATA/>).

626 Moreover, they are grateful to Frederic Frappart for providing the Topex/POSEIDON data.

627 The GSWP2 team is acknowledged for letting the authors use their different forcing fields.

628 The authors also wish to thank one anonymous reviewer who made comments which

629 significantly improved this paper.

630 All the maps have been drawn using the General Mapping Tools.

631 This work has benefited from funding by the ANR, IMPACT BOREAL, and the IPY CARE

632 projects, one of the authors (S. Biancamaria) is supported by a CNES/Noveltis grant.

633

634 References

635

636 Adam, J.C., Haddeland, I., Su, F.G., Lettenmaier, D.P., 2007. Simulation of reservoir  
637 influences on annual and seasonal streamflow changes for the Lena, Yenisei, and Ob' rivers.  
638 Journal of Geophysical Research-Atmospheres 112, D24.

639

640 Akimenko, T.A., Zakharova, E.A., Kouraev, A.V., 2001. Hydrology of the Ob' river system.  
641 Working Paper, INTAS Project 97-3127.

642

643 ArcticRIMS, <http://rims.unh.edu> .

644

645 Arzhanov, M.M., Eliseev, A.V., Demchenko, P.F., Mokhov, I.I., Khon, V.C., 2008.  
646 Simulation of thermal and hydrological regimes of Siberian river watersheds under  
647 permafrost conditions from reanalysis data. Izvestiya Atmospheric and Oceanic Physics  
648 44(1), 83-89.

649

650 Bates, P.D., De Roo, A., 2000. A simple raster-based model for floodplain inundation. Journal  
651 of Hydrology 236, 54-77.

652

653 Beltaos, S., Prowse, T., 2008. River-ice hydrology in a shrinking cryosphere. Hydrological  
654 Processes 23, 122-144.

655

656 Betts, A.K., Beljaars, A.C.M., 2003. ECMWF ISLSCP-II near surface dataset from ERA-40.  
657 ERA-40 Project Report Series 8, [Available from the European Centre for Medium Range  
658 Weather Forecasts, Shinfield Park, Reading, Berkshire RG2 9AX, England], 31 pp.

659  
660  
661  
662  
663  
664  
665  
666  
667  
668  
669  
670  
671  
672  
673  
674  
675  
676  
677  
678  
679  
680  
681  
682  
683

Biancamaria, S., Bates, P.D., Boone, A., Mognard, N., Crétaux, J.-F., 2007. Modelling the Ob river, in western Siberia, using remotely sensed digital elevation models. Proceedings of the « Second Space for Hydrology Workshop », Geneva, 12-14 November 2007, ESA Workshop Proceedings Publication WPP-280.

Boone, A., Masson, V., Meyer, T., Noilhan, J., 2000. The Influence of the Inclusion of Soil Freezing on Simulations by a Soil-Vegetation Atmosphere Transfer Scheme. *Journal of Applied Meteorology* 39, 1544-1569.

Boone, A., Etchevers, P., 2001. An Intercomparison of Three Snow Schemes of Varying Complexity Coupled to the Same Land Surface Model: Local-Scale Evaluation at an Alpine Site. *Journal of Hydrometeorology* 2, 374-394.

Brown, J., Ferrians Jr., O.J., Heginbottom, J.A., Melnikov, E.S., 1998 (revised February 2001). Circum-Arctic map of permafrost and ground-ice conditions. Boulder, CO: National Snow and Ice Data Center/World Data Center for Glaciology, Digital Media.

Chow, V.T., 1964. *Handbook of Applied Hydrology*. McGraw-Hill Book Company, New-York, USA.

Decharme, B., Douville, H., 2006. Uncertainties in the GSWP-2 precipitation forcing and their impacts on regional and global hydrological simulations. *Climate Dynamics* 27, 695–713.

- 684 Decharme, B., Douville, H., 2007. Global validation of the ISBA sub-grid hydrology. *Climate*  
685 *Dynamics* 29(1), 21-37.
- 686
- 687 Dirmeyer, P.A., Gao, X., Zhao, M., Guo, Z., Oki, T., Hanasaki, N., 2006. GSWP-2:  
688 Multimodel Analysis and Implications for Our Perception of the Land Surface. *Bulletin of the*  
689 *American Meteorological Society*, 87, 1381–1397.
- 690
- 691 Etchevers, P., Golaz, C., Habets, F., 2001. Simulation of the water budget and the river flows  
692 of the Rhône basin from 1981 to 1994. *Journal of Hydrology* 244, 60-85.
- 693
- 694 Gorny, A.J., Carter, R., 1987. *World Data Bank II General User's Guide*. Central Intelligence  
695 Agency, Washington, DC, USA.
- 696
- 697 Grabs, W.E., Fortmann, F., De Couuel, T., 2000. Discharge observation networks in Arctic  
698 regions: Computation of the river runoff into the Arctic Ocean, its seasonality and variability.  
699 *The Freshwater Budget of the Arctic Ocean*, E. L. Lewis et al., Eds., Kluwer Academic, 249–  
700 268.
- 701
- 702 Grippa, M., Mognard, N., Le Toan, T., 2005. Comparison between the interannual variability  
703 of snow parameters derived from SSM/I and the Ob river discharge. *Remote Sensing of*  
704 *Environment* 98, 35-44.
- 705
- 706 Habets, F., Noilhan, J., Golaz, C., Goutorbe, J.P., Lacarrère, P., Leblois, E., Ledoux, E.,  
707 Martin, E., Ottlé, C., Vidal-Madjar, D., 1999. The ISBA surface scheme in a macroscale

708 hydrological model applied to the HAPEX-MOBILHY area Part 1: Model and database.  
709 *Journal of Hydrology* 217, 75-96.  
710  
711 Herschy, R.W., Fairbridge, R.W., 1998. *Encyclopedia of Hydrology and Water Resources*, 1<sup>st</sup>  
712 ed., Kluwer Academic Publishers, 572-583.  
713  
714 Huffman, G.J. and Coauthors, 1997. The Global Precipitation Climatology Project (GPCP)  
715 combined precipitation dataset. *Bulletin of the American Meteorological Society* 78, 5–20.  
716  
717 Kanamitsu, M., Ebisuzaki, W., Woollen, J., Yang, S.-K., 2002. NCEP/DOE AMIP-II  
718 reanalysis (R-2). *Bulletin of the American Meteorological Society* 83, 1631–1643.  
719  
720 Manabe, S., Milly, P.C.D., Wetherald, R., 2004. Simulated long-term changes in river  
721 discharge and soil moisture due to global warming. *Hydrological Sciences Journal* 49(4), 625-  
722 642.  
723  
724 Masson, V., Champeaux, J.-L., Chauvin, F., Meriguet, C., Lacaze, R., 2002. A global  
725 database of land surface parameters at 1-km resolution in meteorological and climate models.  
726 *Journal Of Climate* 16(9), 1261-1282.  
727  
728 Meehl, G.A., Stocker, T.F., Collins, W.D., Friedlingstein, P., Gaye, A.T., Gregory, J.M.,  
729 Kitoh, A., Knutti, R., Murphy, J.M., Noda, A., Raper, S.C.B., Watterson, I.G., Weaver, A.J.,  
730 Zhao, Z.-C., 2007. Global Climate Projections. In: *Climate Change 2007: The Physical*  
731 *Science Basis*. Contribution of Working Group I to the Fourth Assessment Report of the  
732 Intergovernmental Panel on Climate Change [Solomon, S., D. Qin, M. Manning, Z. Chen, M.

- 733 Marquis, K.B. Averyt, M. Tignor and H.L. Miller (eds.)]. Cambridge University Press,  
734 Cambridge, United Kingdom and New York, NY, USA.  
735
- 736 Nohara, D., Kitoh, A., Hosaka, M., Oki, T., 2006. Impact of climate change on river discharge  
737 projected by multimodel ensemble. *Journal of Hydrometeorology* 7(5), 1076-1089.  
738
- 739 Noilhan, J., Lacarrère, P., 1995. GCM Grid-Scale Evaporation from Mesoscale Modeling.  
740 *Journal of Climate* 8(2), 206–223.  
741
- 742 Noilhan, J., Mahfouf, J.-F., 1996. The ISBA land surface parametrisation scheme. *Global and*  
743 *Planetary Change* 13, 145-159.  
744
- 745 Oki, T., Sud, Y.C., 1998. Design of Total Runoff Intergrating Pathways (TRIP) – A Global  
746 River Channel Network. *Earth interactions* 2.  
747
- 748 Pavelsky, T.M., Smith, L.C., 2004. Spatial and temporal patterns in Arctic river ice breakup  
749 observed with MODIS and AVHRR time series. *Remote Sensing of Environment* 93, 328-  
750 338.  
751
- 752 Peters, D.L., Prowse, T.D., Pietroniro, A., Leconte, R., 2006. Flood hydrology of the Peace-  
753 Athabasca Delta, northern Canada. *Hydrological Processes* 20, 4073-4096.  
754
- 755 Peterson, B.J., Holmes, R.M., McClelland, J.W., Vörösmarty, C.J., Lammers, R.B.,  
756 Shiklomanov, A.I., Shiklomanov, I.A., Rahmstorf, S., 2002. Increasing river discharge to the  
757 Arctic Ocean. *Science* 298(5601), 2171–2173.

758

759 Pitman, A.J., Yang, Z-L., Cogley, J.G., Henderson-Sellers, A., 1991. Description of bare  
760 essentials of surface transfer for the bureau of meteorology research centre AGCM. BMRC  
761 Research Report No. 32, various pagings.

762

763 Prowse, T. D., 2001. River-ice ecology: I. Hydrologic, geomorphic, and water-quality aspects.  
764 *Journal of Cold Regions Engineering* 15 (1), 1 – 16.

765

766 Rudolf, B., Hauschild, H., Reuth, W., Schneider, U., 1994. Terrestrial precipitation analysis:  
767 Operational method and required density of point measurements. *Global Precipitation and*  
768 *Climate Change*, M. Desbois and F. Desalmond, Eds., NATO ASI Series I 26, Springer-  
769 Verlag, 173–186.

770

771 Serreze M. C., Bromwich, D.H., Clark, M.P., Etringer, A.J., Zhang, T., Lammers, R., 2002.  
772 Large-scale hydro-climatology of the terrestrial Arctic drainage system. *Journal of*  
773 *Geophysical Research* 108, doi:10.1029/2001JD000919.

774

775 Shiklomanov, A.I., Lammers, R.B., Vörösmarty, C.J., 2002. Widespread decline in  
776 hydrological monitoring threatens panarctic research. *EOS Transactions, American*  
777 *Geophysical Union* 83 (2), 13.

778

779 Smith, L.C., Alsdorf, D.E., 1998. Control on sediment and organic carbon delivery to the  
780 Arctic Ocean revealed with space-borne synthetic aperture radar: Ob' River, Siberia. *Geology*  
781 26 (5), 395-398.

782

- 783 Su, F.G., Adam, J.C., Trenberth, K.E., Lettenmaier, D.P., 2006. Evaluation of surface water  
784 fluxes of the pan-Arctic land region with a land surface model and ERA-40 reanalysis.  
785 *Journal of Geophysical Research-Atmospheres* 11, D5.  
786
- 787 Versegny, D.L., 1991. CLASS - A Canadian land surface scheme for GCMs. I. Soil Model.  
788 *International Journal of Climatology* 11, 111-133.  
789
- 790 Vuglinsky, V.S., 2001. Peculiarities of ice events in Russian Arctic rivers. *Hydrological*  
791 *Processes* 16, 905-913.  
792
- 793 Wilson, M., Bates, P.D., Alsdorf, D., Forsberg, B., Horritt, M., Melack, J., Frappart, F.,  
794 Famiglietti, J., 2007. Modeling large-scale inundation of Amazonian seasonally flooded  
795 wetlands. *Geophysical Research Letters* 34, L15404, doi:10.1029/2007GL030156.  
796
- 797 Wu, T., W., G., 2004. An empirical formula to compute snow cover fraction in GCMs.  
798 *Advances in Atmospheric Sciences* 21, 529-535.  
799
- 800 Yang, D., Ye, B., Shiklomanov, A., 2004. Discharge Characteristics and Changes over the Ob  
801 River Watershed in Siberia. *Journal of hydrometeorology* 5, 595-610.  
802
- 803 Yang, D., Zhao, Y., Armstrong, R., Robinson, D., Brodzik, M.-J., 2007. Streamflow response  
804 to seasonal snow cover mass changes over large Siberian watersheds. *Journal of Geophysical*  
805 *Research* 112, doi:10.1029/2006JF000518.  
806

807 Yang, Z.-L., Dickinson, R.E., Robock, A., Vinnikov, K.Y., 1997. Validation of snow sub-  
808 model of the biosphere-atmosphere transfer scheme with Russian snow-cover and  
809 meteorological observations data. *Journal of Climate* 10, 353-373.

810 Table captions

811

812 Table 1. GSWP2 experiments with the reanalysis used as precipitation forcing and the applied

813 correction(s)

814

815 Table 2. Correlation coefficient, bias, RMSE and Nash-Sutcliffe coefficient between

816 measured and modelled discharge at Salekhard for different precipitation datasets and for

817  $c_{pn}=0.01$ ,  $w_{drain}=0.02$  and  $Z_{0new}$

818

819 Table 3. Correlation coefficient and Nash-Sutcliffe coefficient between modelled and in-situ

820 discharge at Salekhard for different values of the river depth (m) and the Manning coefficient

821 (bold numbers correspond to GSWP2-P4 and non-bold numbers correspond to GSWP2-P3)

822

823 Table 4. Mean RMSE between Topex/POSEIDON and modelled water heights for GSWP2-

824 P3 and GSWP2-P4

825 Figure captions

826

827 Fig. 1. Study domain (Lower Ob). The red arrows represent the lateral inflows to the  
828 hydraulic model, the green arrow represents the boundary condition (from the Belogorje  
829 gauging station), the blue line represents the water mask used to describe the river in the  
830 hydraulic model

831

832 Fig. 2. Models used in this study and their interactions (LISFLOOD-FP is a flood inundation  
833 model, ISBA is a Land Surface Scheme and TRIP is a routing scheme)

834

835 Fig. 3. Routing scheme used to compute the lateral inflows to the river from the ISBA study  
836 domain (the lateral inflow number, see Fig. 1, is indicated in red). The blue dots represent the  
837 pixels on the lower Ob and the yellow dots, each ISBA grid cell which contributes to the  
838 lateral inflow

839

840 Fig. 4. River bathymetry (red curve) computed from a filtered topography (magenta curve)  
841 derived from the ACE DEM elevation along the river (blue dots)

842

843 Fig. 5. DEMs available on the study domain: GTOPO30 (from USGS) and ACE (from De  
844 Montfort University). The ACE DEM has been chosen for our study.

845

846 Fig. 6. In-situ discharge at Belogorje with a time lag of 10 days and in-situ discharge at  
847 Salekhard with no time-lag; their difference gives an estimate of the total lateral inflow to the  
848 river between the two gages (a.). This "in-situ" total lateral inflow is compared to the sum of  
849 the ISBA lateral inflows (b.). The eight modelled lateral inflows are also shown (c.)

850

851 Fig. 7. Modelled lateral inflow  $Q$  from ISBA (blue dashed line on all plots) compared to  
 852 (red curves) rain precipitation rate (a.), snow precipitation rate (b.), evapotranspiration (c.),  
 853 snow fraction (d.), air temperature (e.), temperature in the first soil layer (f.), liquid water  
 854 equivalent soil ice (g.) and soil liquid water (h.). These plots correspond to a spatial average  
 855 on all ISBA grid cells contributing to lateral inflow  $Q$  (see Fig. 3)

856

857 Fig. 8. Soil/vegetation roughness length ( $Z_0$ ) and vegetation cover (VEG) averaged for all the  
 858 ISBA grid cells contributing to lateral inflow  $Q$  (a.). Modelled snow fraction on vegetation  
 859 ( $p_{nc}$ ) and on bare soil ( $p_{ng}$ ) are also shown (b.)

860

861 Fig. 9. Total lateral inflow from in-situ measurement (cyan curve) compared to modelled total  
 862 lateral inflow for  $c_{pn}$  equal to 5, 1, 0.1, 0.01 and 0.001 and for roughness length equal to  $Z_0$   
 863 (a.) and  $Z_{0new}$  (b.)

864

865 Fig. 10. Sum of modelled lateral inflows for  $w_{drain}=0, 0.01, 0.02, 0.03$  and  $0.05$  with  
 866  $c_{pn}=0.01$  and roughness length equal to  $Z_{0new}$

867

868 Fig. 11. Sum of all lateral inflows for all the GSWP2 precipitation datasets for  $c_{pn}=5$ ,  
 869  $w_{drain}=0$  and  $Z_0$  (nominal run, a.) and for  $c_{pn}=0.01$ ,  $w_{drain}=0.02$  and  $Z_{0new}$  (b.). Modelled  
 870 discharge at Salekhard for all the GSWP2 precipitation datasets for  $c_{pn}=5$ ,  $w_{drain}=0$  and  $Z_0$   
 871 (c.) and for  $c_{pn}=0.01$ ,  $w_{drain}=0.02$  and  $Z_{0new}$  (d.)

872

873 Fig. 12. Modelled discharge at Salekhard for different values of the river depth (5m, 10m and  
 874 15m) and for a Manning coefficient of 0.015 (a. and c.). Modelled discharge at Salekhard for

875 different values of the Manning coefficient (0.01, 0.015, 0.02 and 0.025) and for a river depth  
876 of 10m (b. and d.). Plots a. and b. are obtained with lateral inflows computed using GSWP2-  
877 P3 precipitation field, whereas plots c. and d. are obtained with GSWP2-P4 precipitation  
878 dataset. On each plot, the blue curve corresponds to the observed discharge at Salekhard  
879

880 Fig. 13. Location of the different Topex/Poseidon virtual stations used

881

882 Fig. 14. Comparison between Topex/POSEIDON measured water height (red curves on the  
883 two plots) and modelled water height with GSWP2-P3 (magenta dashed curve) and with  
884 GSWP2-P4 (black curve) for a river depth of 10m and a Manning coefficient of 0.015 at the  
885 location of virtual stations n°4 (a.), n°9 (b.), n°17 (c.) and n°24 (d.) (see Fig. 13 for their  
886 location)

887 Table 5 :  
888

GSWP2 experiment	Reanalysis	Hybridization	Gauge correction
B0	NCEP/DOE	Yes (GPCC and GPCP)	Yes
P1	ERA-40	No	No
P2	NCEP/DOE	Yes (GPCC)	Yes
P3	NCEP/DOE	Yes (GPCC)	No
P4	NCEP/DOE	No	No
PE	ERA-40	Yes (GPCC and GPCP)	No

889 Table 2:  
890

Precipitation ISBA input	Model vs observation			
	Correlation coefficient	Bias (m <sup>3</sup> /s)	RMSE (m <sup>3</sup> /s)	Nash-Sutcliffe coefficient
GSWP2-B0	0.97	-1571	3 554	0.88
GSWP2-P1	0.99	700	2 157	0.96
GSWP2-P2	0.96	-2797	5 183	0.75
GSWP2-P3	0.99	674	1 917	0.97
GSWP2-P4	0.99	-1363	2 289	0.95
GSWP2-PE	0.98	-912	2 607	0.94

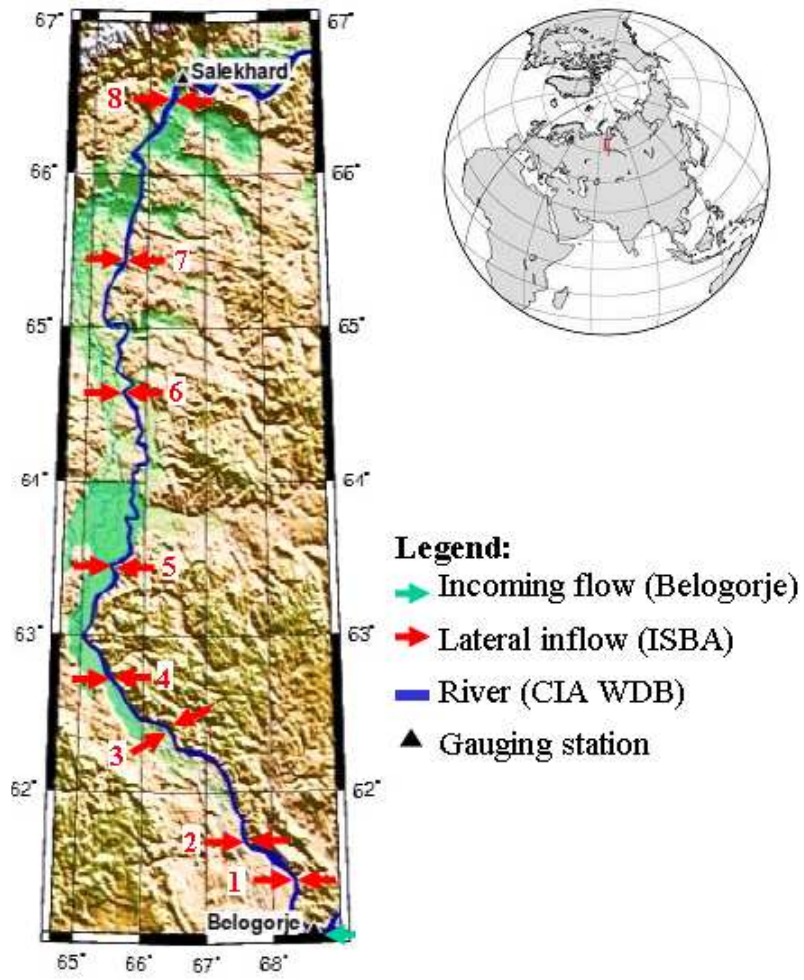
891 Table 3:  
892

River depth (m)	Manning coefficient	Correlation coefficient	RMSE (m <sup>3</sup> /s)	Nash-Sutcliffe
5	0.01	0.86 <b>0.88</b>	5 393 <b>5 310</b>	0.74 <b>0.75</b>
	0.015	0.56 <b>0.59</b>	8 920 <b>8 924</b>	0.28 <b>0.28</b>
	0.02	0.25 <b>0.30</b>	10 982 <b>11 032</b>	-0.09 <b>-0.10</b>
	0.025	-0.0002 <b>0.06</b>	12 105 <b>12 029</b>	-0.32 <b>-0.30</b>
10	0.01	0.98 <b>0.96</b>	2 263 <b>3 510</b>	0.95 <b>0.89</b>
	0.015	0.99 0.99	2 136 2 409	0.96 0.95
	0.02	0.89 <b>0.88</b>	4 861 <b>5 248</b>	0.79 <b>0.75</b>
	0.025	0.71 <b>0.70</b>	7 423 <b>7 833</b>	0.50 <b>0.45</b>
15	0.01	0.98 <b>0.95</b>	2 508 <b>3 951</b>	0.94 <b>0.86</b>
	0.015	0.98 <b>0.97</b>	2 131 <b>3 405</b>	0.96 <b>0.90</b>
	0.02	0.99 <b>0.98</b>	1 956 <b>2 722</b>	0.97 <b>0.93</b>
	0.025	0.98 <b>0.98</b>	2 489 <b>2 595</b>	0.94 <b>0.94</b>

893 Table 4:  
894

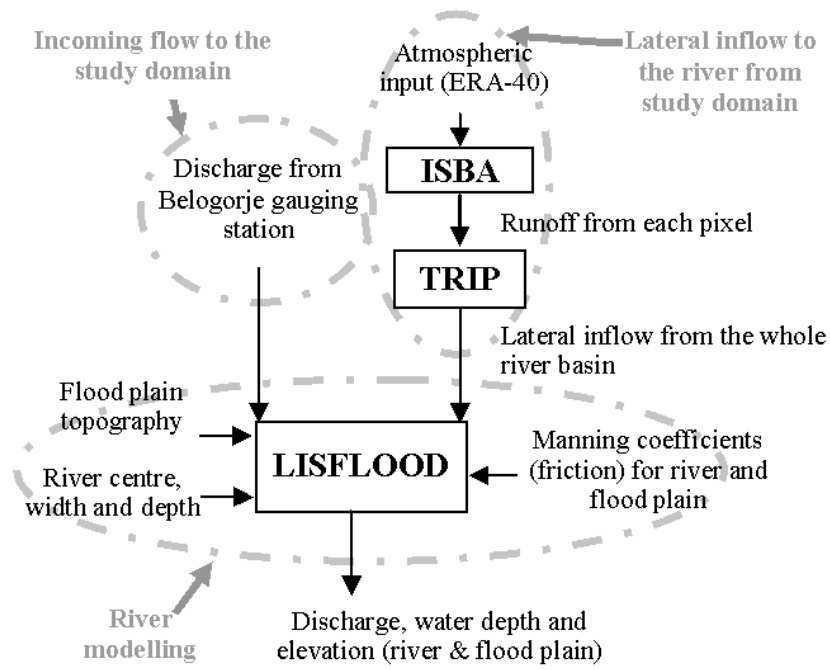
Precipitation	Topex station	Mean RMSE modelled/Topex water height (m)	
		RD=10m Cman=0.015	RD=15m Cman=0.020
GSWP2-P3	All stations	2.6	5.7
	Station n°4	1.7	4.4
	Station n°9	2.3	4.9
	Station n°17	2.0	5.1
	Station n°24	3.2	6.2
GSWP2-P4	All stations	2.0	4.6
	Station n°4	1.1	3.5
	Station n°9	1.6	3.9
	Station n°17	1.2	4.0
	Station n°24	2.2	5.0

895 Figure 1:  
896



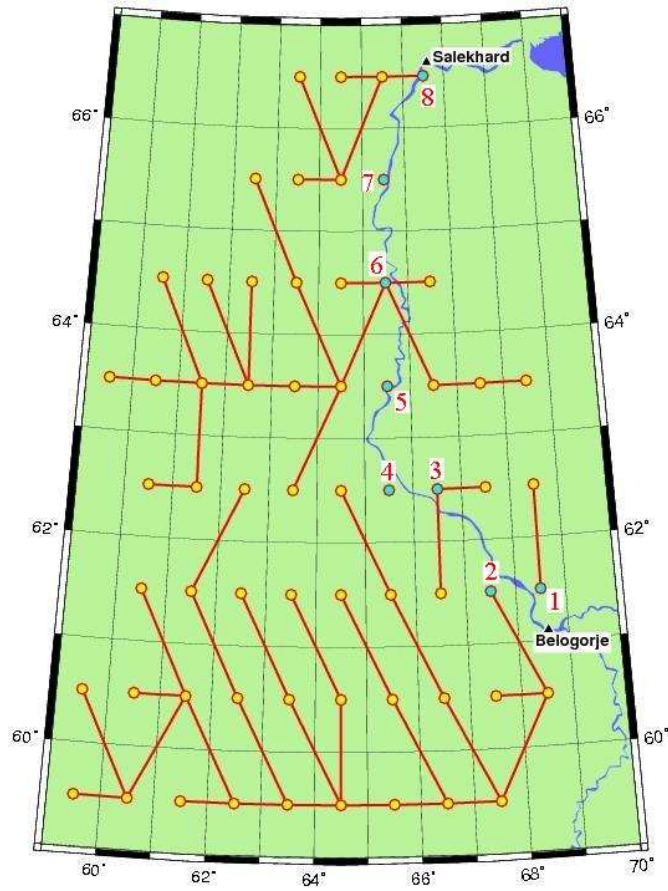
897

898 Figure 2:  
899



900

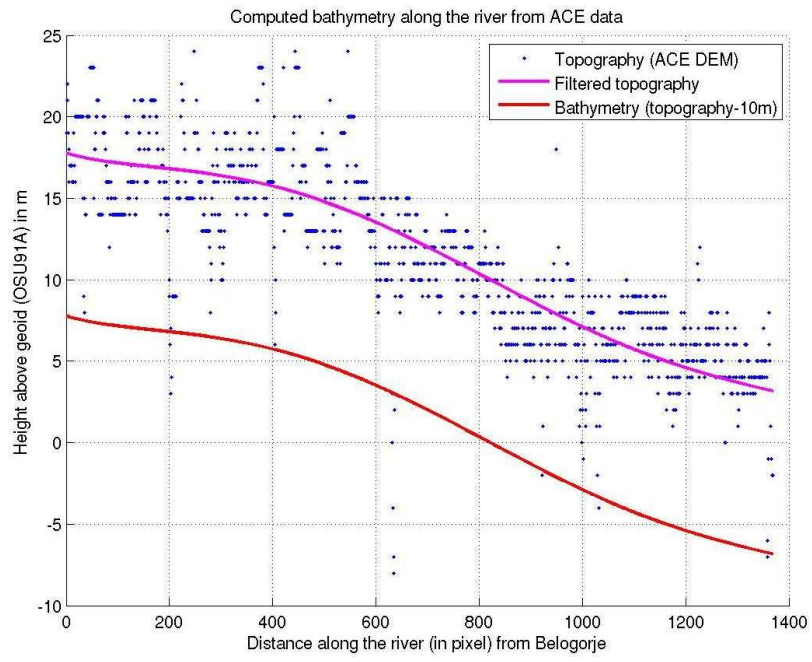
901 Figure 3:  
902



903

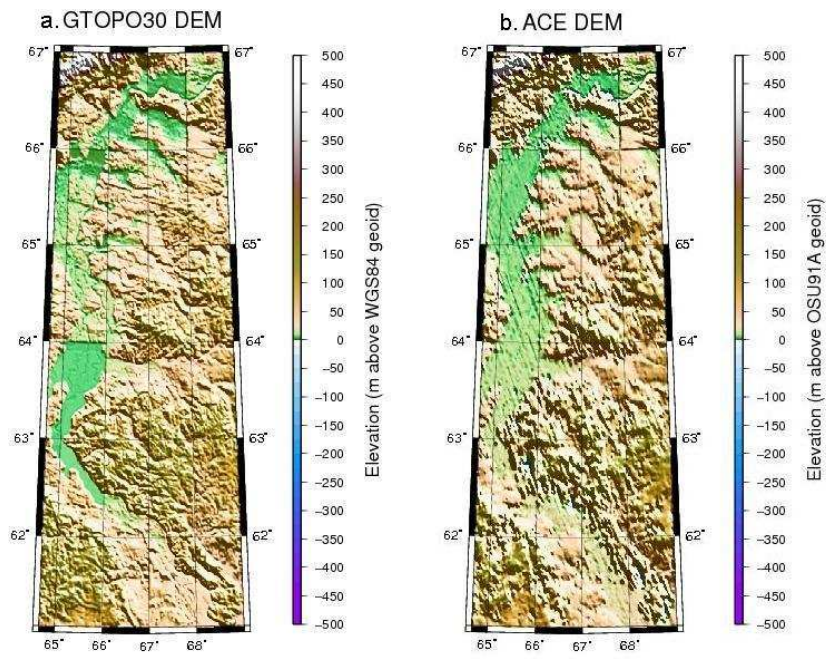
hal-00575483, version 1 - 10 Mar 2011

904 Figure 4:  
905



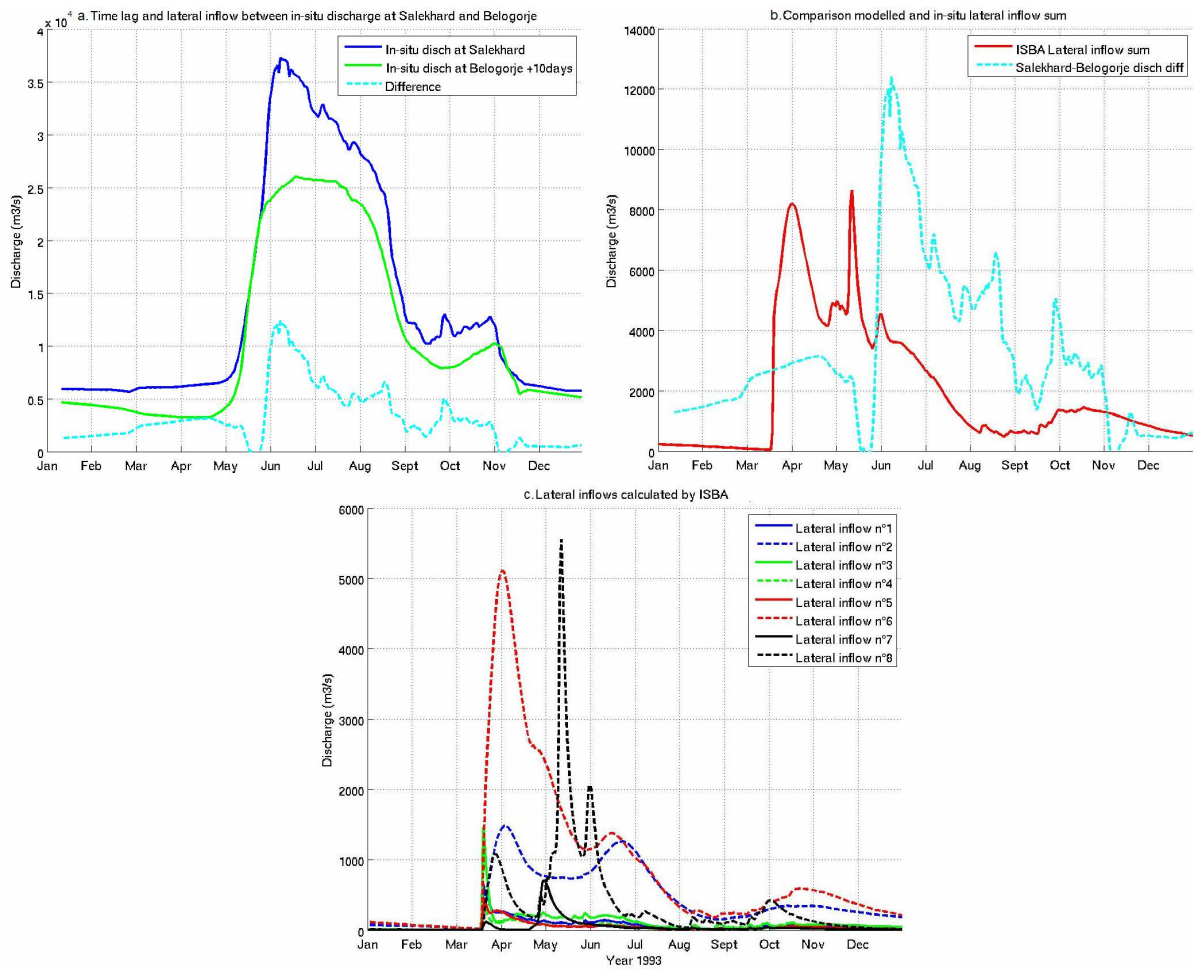
906

907 Figure 5:  
908



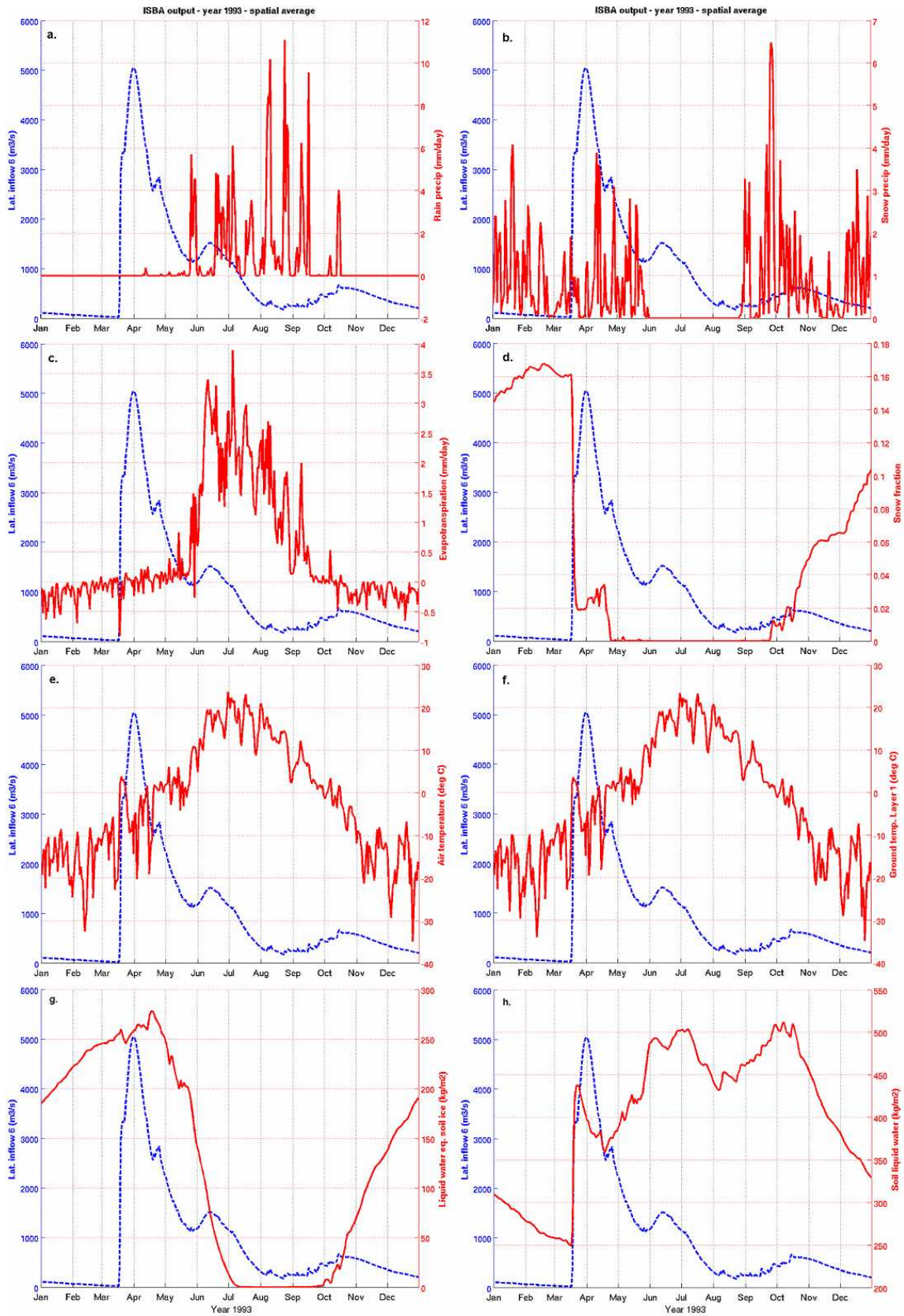
909

910 Figure 6:  
911



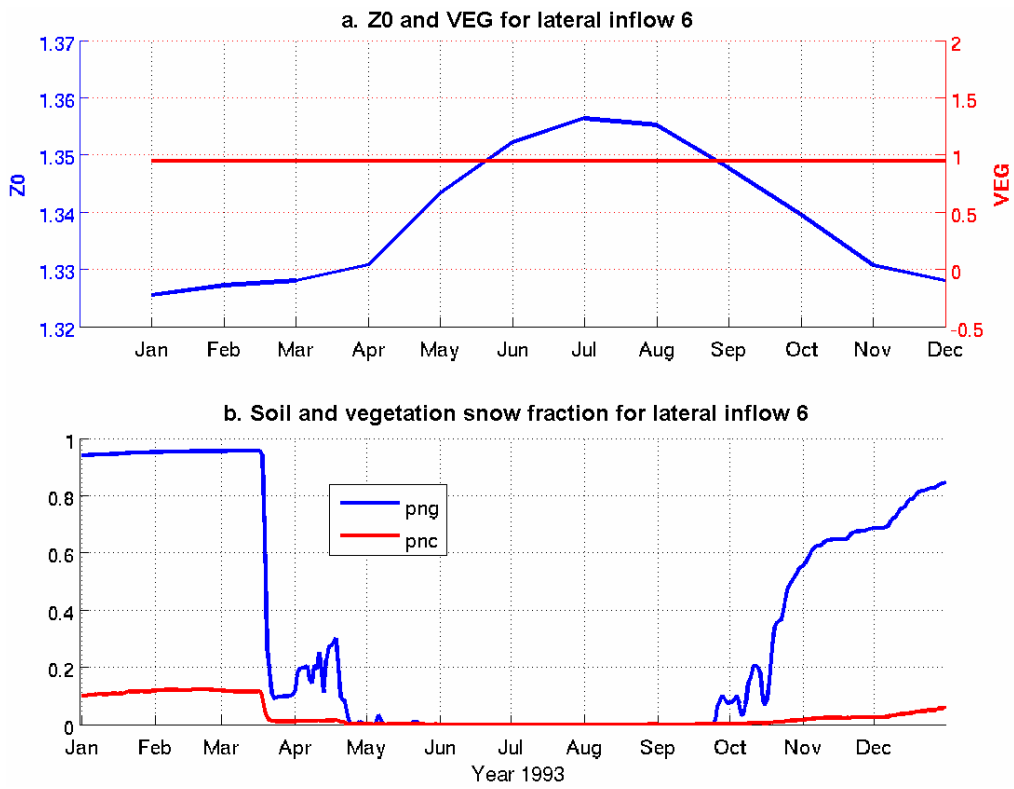
912

913 Figure 7:  
914



915

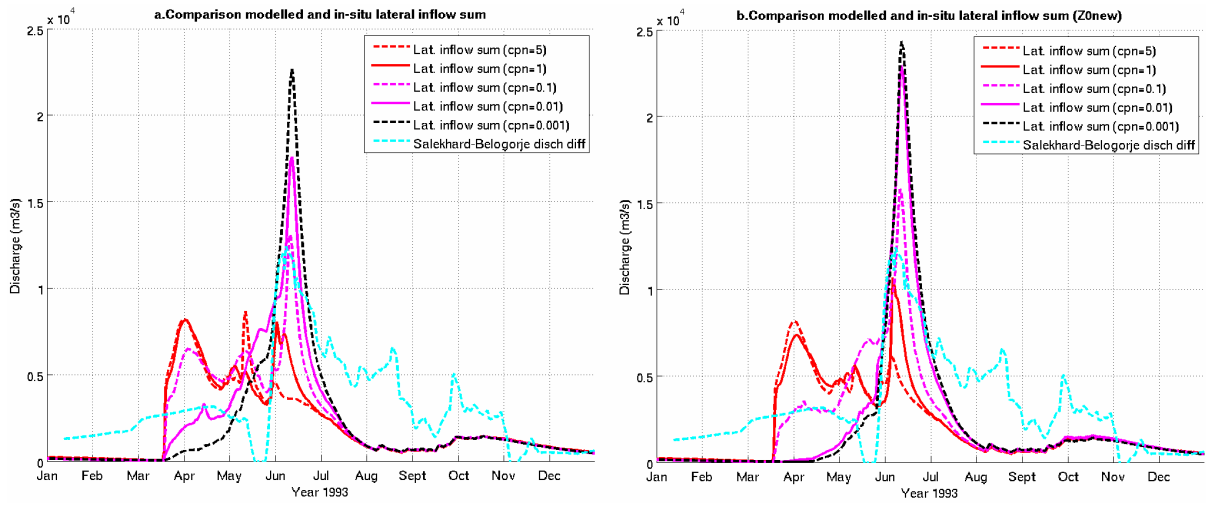
916 Figure 8:  
917



918  
919

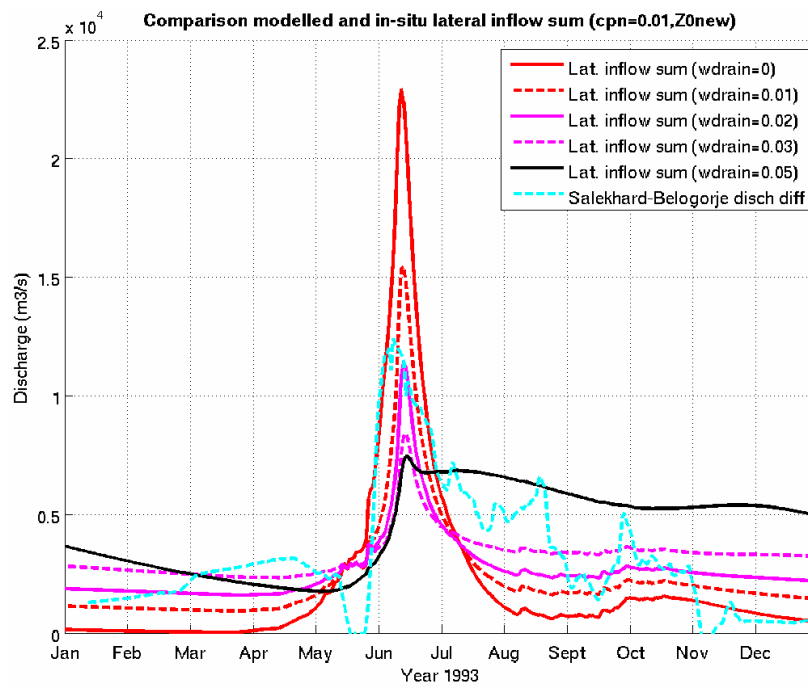
920  
921  
922

Figure 9:



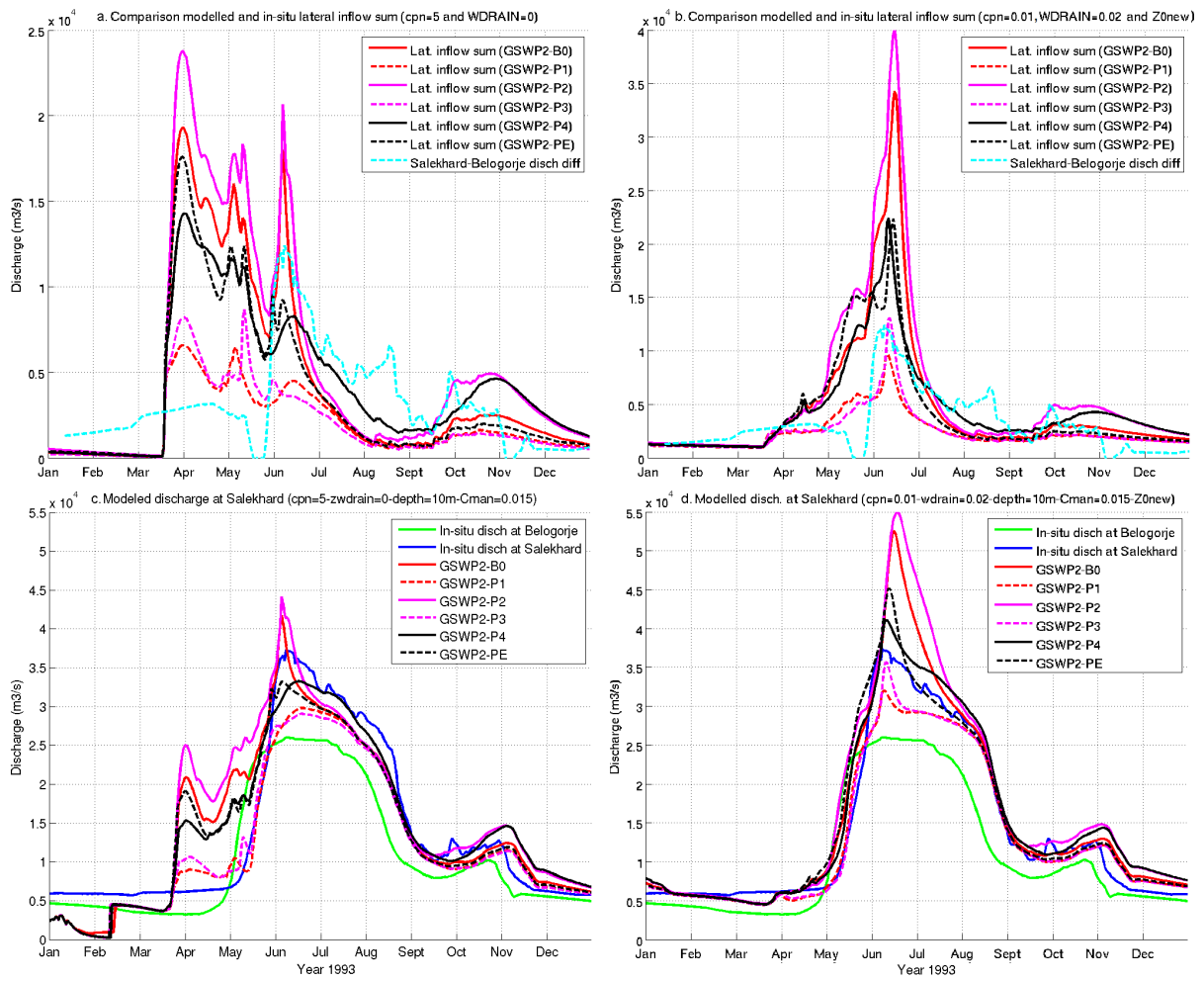
923

924 Figure 10:  
925



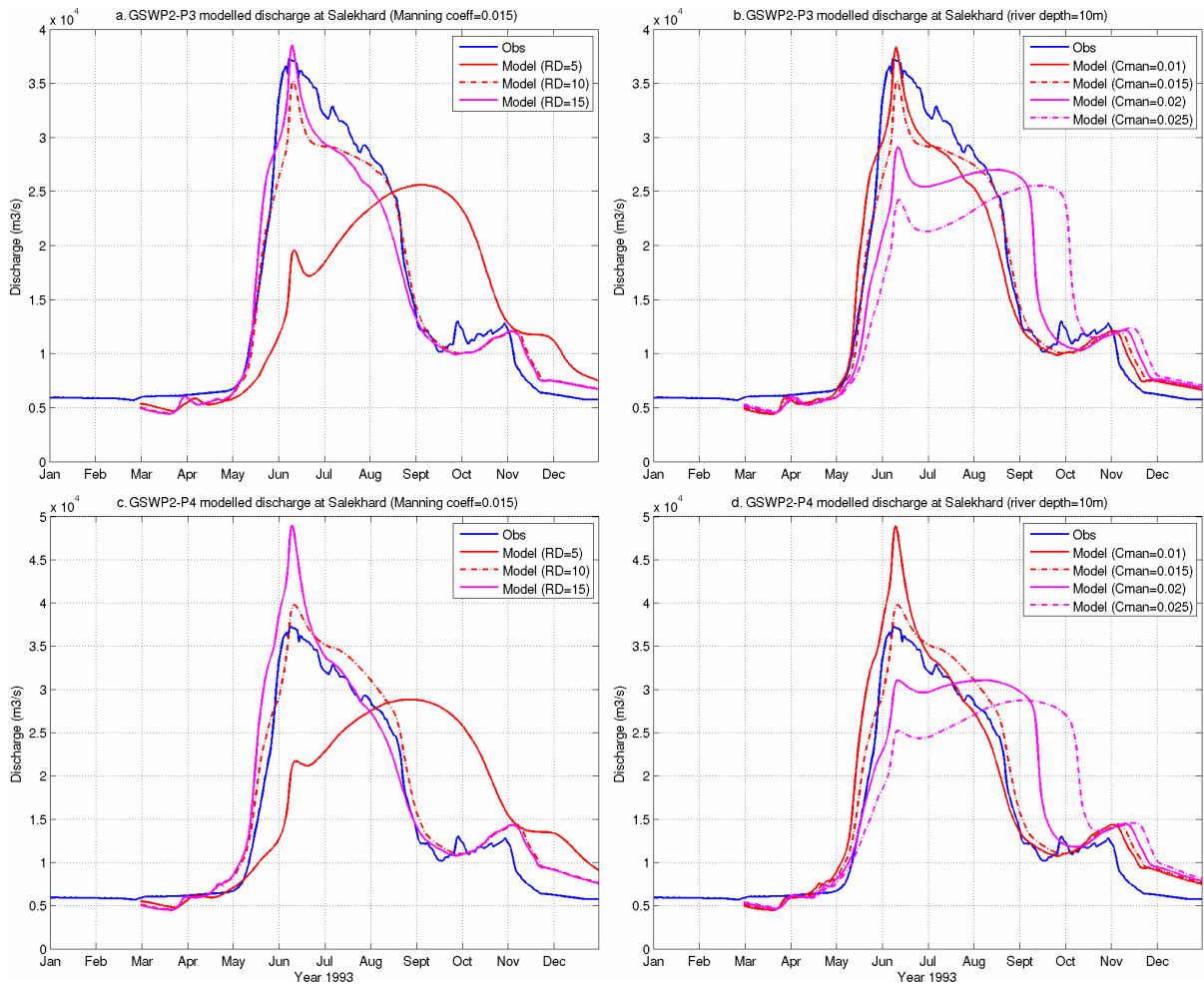
926

927 Figure 11:  
928



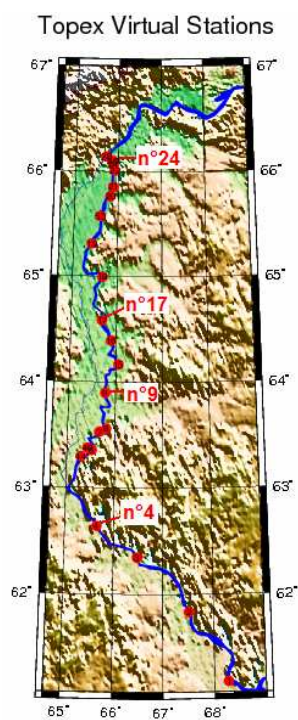
929

930 Figure 12:  
931



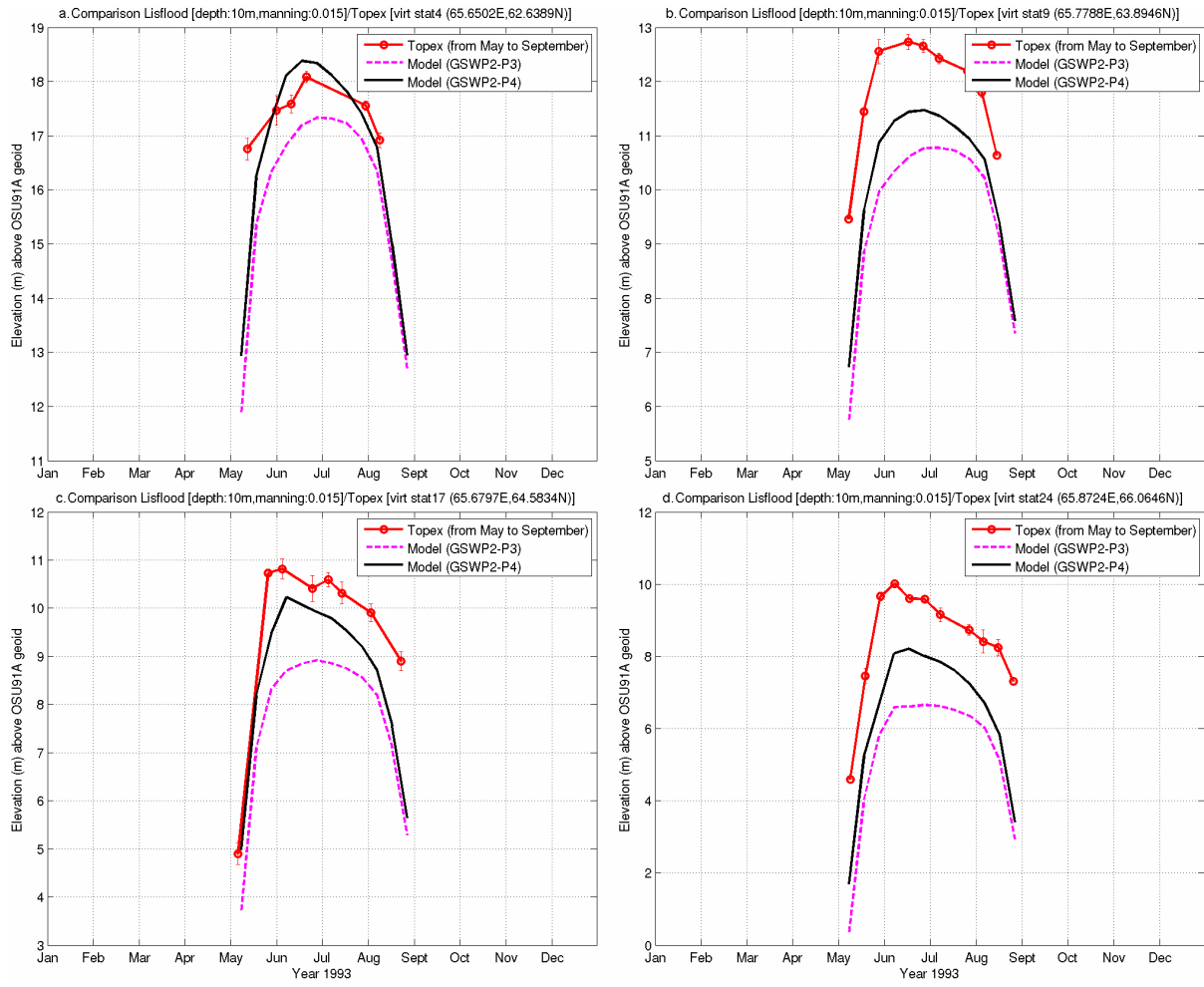
932

933 Figure 13:  
934



935

936 Figure 14:  
937



938  
939

hal-00575483, version 1 - 10 Mar 2011